Horizontally Polarized Kink Oscillations Supported by Solar Coronal Loops in an Asymmetric Environment

Mijie Shi[1], Bo Li[1], and Shengju Yuan[2]

[1] Shandong Key Laboratory of Optical Astronomy and Solar-Terrestrial Environment, School of Space Science and Physics, Institute of Space Sciences, Shandong University, Weihai, Shandong, 264209, China
e-mail: `shimijie@sdu.edu.cn`

[2] Institute of Frontier and Interdisciplinary Science, Shandong University, Qingdao, Shandong, 266237, China

ABSTRACT

Context. Kink oscillations are ubiquitously observed in solar coronal loops, their understanding being crucial in the contexts of coronal seismology and atmospheric heating.

Aims. We study kink modes supported by a straight coronal loop embeded in an asymmetric environment using three-dimensional magnetohydrodynamic (MHD) simulations.

Methods. We implement the asymmetric effect by setting different exterior densities below and above the loop interior, and initiate the simulation using a kink-like velocity perturbation perpendicular to the loop plane, mimicking the frequently measured horizontally polarized kink modes.

Results. We find that the external velocity fields show fan blade structures propagating in the azimuthal direction as a result of the successive excitation of higher azimuthal Fourier modes. Resonant absorption and phase mixing can still occur despite an asymmetric environment, leading to the development of small scales at loop boundaries. These small scales nonetheless develop asymmetrically at the upper and lower boundaries due to the different gradients of the Alfvén speed.

Conclusions. These findings enrich our understanding of kink modes in coronal loops embedded within an asymmetric environment, providing insights helpful for future high-resolution observations.

Key words. sun:corona – sun: magnetic fields

1. Introduction

Magnetohydrodynamic (MHD) waves abound in the solar atmosphere (see reviews by, e.g., Li et al. 2020; Van Doorsselaere et al. 2020; Banerjee et al. 2021; Nakariakov et al. 2021; Wang et al. 2021). In particular, kink waves supported by the structured corona have attracted considerable attention since their first imaging detection (Aschwanden et al. 1999; Nakariakov et al. 1999). Further observations show that kink oscillations in coronal loops may be decaying (e.g., Zimovets & Nakariakov 2015; Goddard et al. 2016) or decayless (Tian et al. 2012; Wang et al. 2012; Nisticò et al. 2013; Anfinogentov et al. 2015). Ubiquitous propagating kink modes were also detected in the outer corona (Tomczyk et al. 2007; Van Doorsselaere et al. 2008). Studies of kink modes are often placed in the context of either coronal heating or coronal magnetic field diagnosis (e.g., Nakariakov & Ofman 2001; Yang et al. 2020). The two contexts are not mutually exclusive. As an example, Goddard & Nisticò (2020) connected the evolution of kink waves with the thermal evolution of their host loops.

A thorough understanding of kink modes is crucial for their applications. In classical theories where a straight coronal loop and a piecewise constant loop interior and exterior are assumed, kink modes are a collective eigenmode with azimuthal wavenumber $q = 1$ (e.g., Edwin & Roberts 1983). When a continuous transition layer connects the loop interior and exterior, kink modes are subject to resonant absorption (Goossens et al. 2011). During this process, the coordinated wave energy is transferred to localized Alfvénic motions, which subsequently phase-mix to generate small scales. Along this line of thinking, a variety of modeling works have been performed to explore either the properties of kink modes or their heating effects (e.g., Antolin et al. 2015; Magyar & Van Doorsselaere 2016; Karampelas et al. 2017; Guo et al. 2019, 2020; Shi et al. 2021b,a; De Moortel & Howson 2022).

In reality, however, the environment of coronal loops is unlikely to be uniform. Take the much-studied horizontally polarized kink modes (Wang et al. 2008). The upper and lower ambient coronae of the loop apex may be asymmetric due to density stratification. While the properties of MHD waves in an asymmetric slab configuration have been examined (e.g., Allcock & Erdélyi 2017; Zsámberger et al. 2018; Chen et al. 2022), there exists no dedicated study on collective waves supported by an asymmetric tube. This work examines the property of kink modes supported by a straight coronal loop in an asymmetric environment using 3D MHD simulations. New features are revealed in comparison with the case where a symmetric ambient corona is implemented. Section 2 provides the numerical setup, followed by the simulation results in Section 3. Section 4 is the summary.

2. Numerical setup

Our equilibrium configuration, illustrated in Figure 1(b), is a straightened version of a curved tube anchored in the photosphere (Figure 1(a)). We see coronal loops as field-aligned magnetic tubes. The equilibrium magnetic field is z-directed, and all equilibrium quantities are z-independent. The

equilibrium density is prescribed by

$$\rho(x, y) = \rho_e(\theta) + [\rho_i - \rho_e(\theta)] f(r), \qquad (1)$$

where (r, θ) denotes a standard polar coordinate system in the $x - y$ plane and the azimuthal coordinate θ is measured counter clockwise from the positive direction of the x-axis. A continuous profile $f(r) = \exp[-(r/R)^\alpha]$ is used to connect the internal density $\rho_i = 5 \times 10^8 m_p \mathrm{cm}^{-3}$ (m_p is the proton mass) to some external density $\rho_e(\theta)$, with $\alpha = 6$ and the nominal loop radius $R = 1$ Mm. This setup makes the length of the transition layer l normalised to the loop radius as $l/R \approx 0.6$, which is within the range of some seismological estimation based on resonant absorption (e.g., Arregui et al. 2007). We construct an asymmetric background (hereafter the asymmetric case) by setting

$$\rho_e(\theta) = \rho_{e1} + (\rho_{e2} - \rho_{e1})\frac{1 - \sin\theta}{2}, \qquad (2)$$

where $[\rho_{e1}, \rho_{e2}] = [1, 3.5] \times 10^8 m_p \mathrm{cm}^{-3}$. Here ρ_{e1} represents the density at $(x, y) = (0, +\infty)$ and ρ_{e2} at $(x, y) = (0, -\infty)$. Figures 2(a2) and 2(b2) show the equilibrium density profiles along the x-axis (i.e., $y = 0$) and y-axis (i.e., $x = 0$) for this case. One sees that the loop environment is asymmetric along the y-direction but symmetric along the x-direction. The x-(y-) direction is seen as horizontal (vertical) in accordance with the convention in naming the polarization properties of kink motions (see Figure 1(a)). The magnetic field is set to be uniform (15 G). The interior temperature at $(x, y) = (0, 0)$ is $T_i = 1$ MK. A uniform thermal pressure is implemented to enforce transverse force balance, the resulting plasma β being 0.0155. The pertinent Alfvén speeds are $[v_{Ai}, v_{Ae1}, v_{Ae2}] = [1463, 3272, 1749]$ km s^{-1}. The loop length is $L = 50$ Mm. A further simulation with the symmetric background ($\rho_{e1} = \rho_{e2} = 1 \times 10^8 m_p \mathrm{cm}^{-3}$, hereafter the symmetric case) is conducted for comparison (Figures 2(a1) and (b1)).

For both cases, the equilibrium is perturbed by a horizontal kick

$$v_x(x, y, z; t = 0) = v_0 \exp\left(-\frac{r^2}{2\sigma^2}\right) \sin\left(\frac{\pi z}{L}\right), \qquad (3)$$

where $v_0 = 10$ km s^{-1} is the amplitude, and $\sigma = R$ characterizes the spatial extent. The z-dependence in Equation (3) dictates that only axial fundamentals are of interest here.

The set of ideal MHD equations is evolved using the PLUTO code (Mignone et al. 2007). We use the piecewise parabolic method for spatial reconstruction, and the second-order Runge–Kutta method for time-stepping. The Harten-Lax-van Leer Discontinuities (HLLD) approximate Riemann solver (Miyoshi & Kusano 2005) is used for computing inter-cell fluxes, and a hyperbolic divergence cleaning method is used to keep the magnetic field divergence-free. We simulate only half of the loop by taking advantage of the symmetry with respect to the apex plane ($z = L/2$). The simulation domain is $[-20, 20]$Mm $\times [-20, 20]$Mm $\times [0, 25]$Mm in x, y, and z. In the x- and y-direction, we use 600 uniform grids for $[-4, 4]$Mm and 200 stretched grids in the rest. A uniform grid with 50 cells is adopted in the z-direction. We use the outflow boundary condition for all prim-
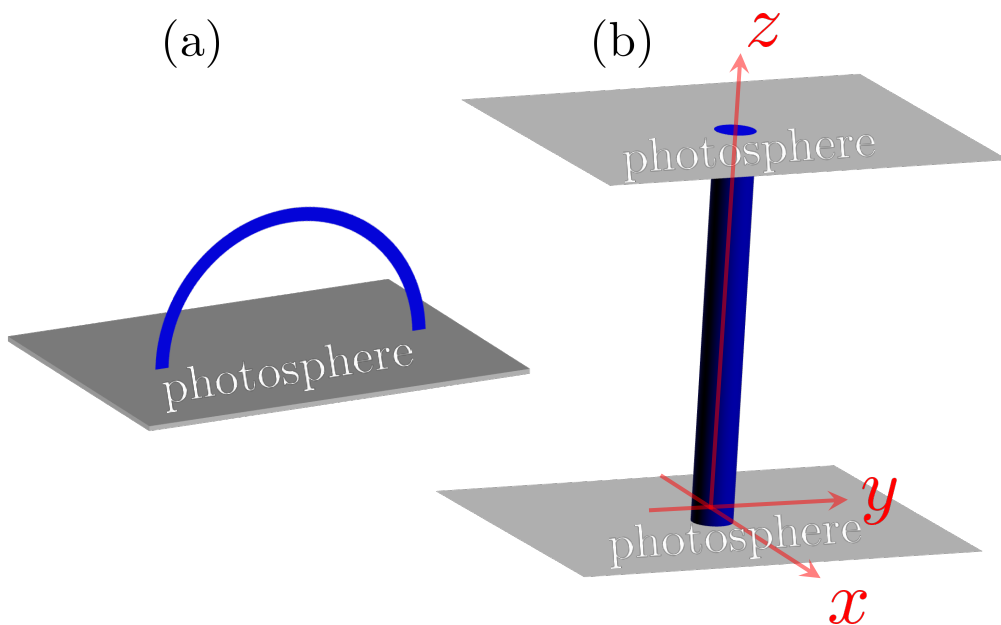
Fig. 1. Illustrations of (a) a curved tube anchored in the photosphere and (b) its straightened version used in our configuration.
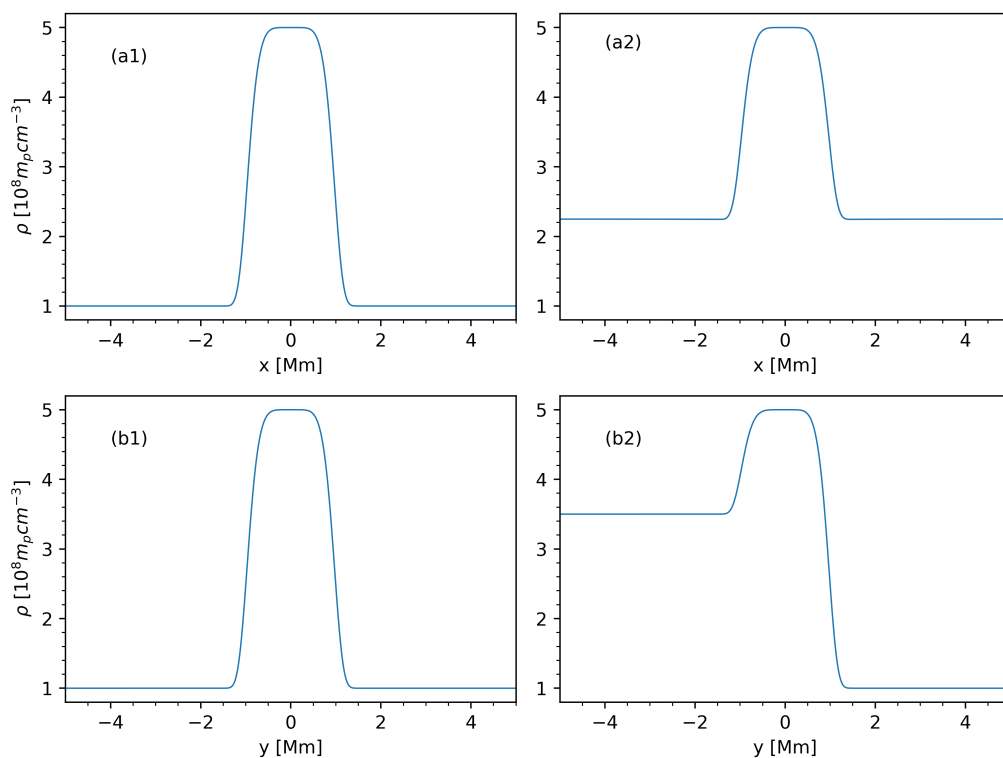

Fig. 2. Equilibrium density profiles along the x-axis ($y = 0$) and y-axis ($x = 0$) for the symmetric (left) and asymmetric case (right).

itive variables at the lateral boundaries (x and y). Symmetric boundary condition is applied at the top boundary ($z = L/2$). For the bottom boundary ($z = 0$), the transverse velocities (v_x and v_y) are
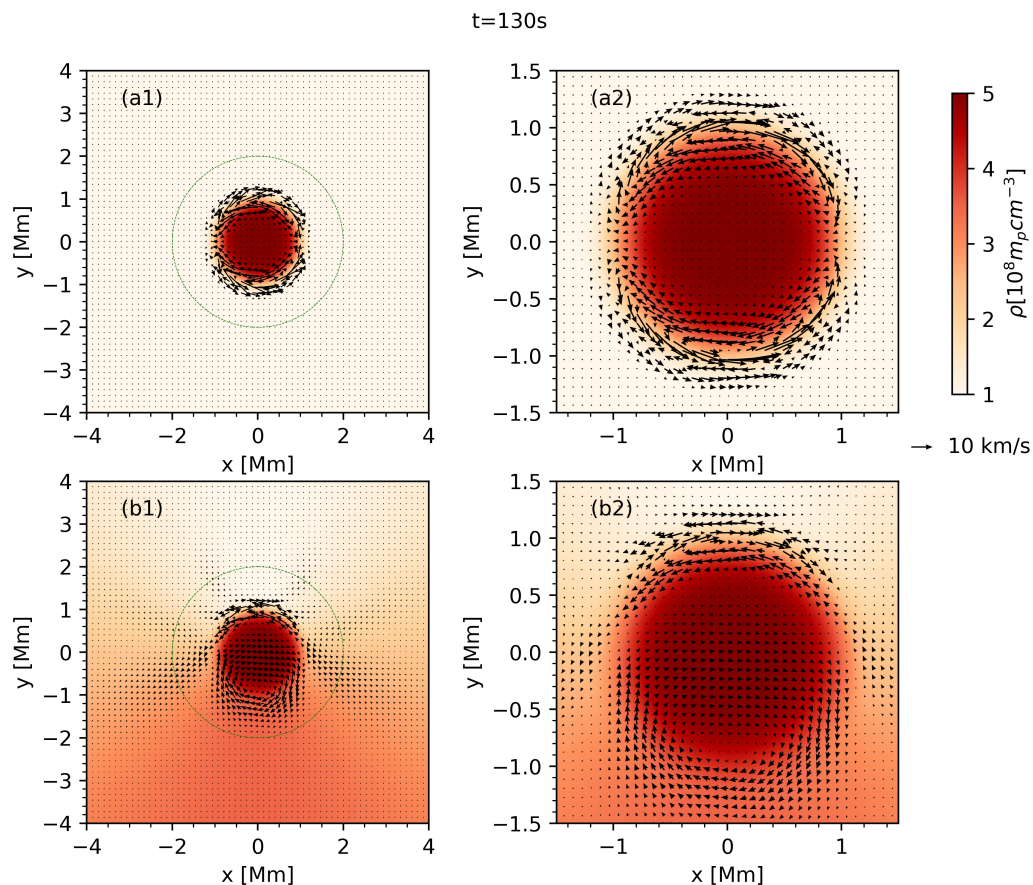
Fig. 3. Density distributions and velocity fields at the loop apex for the symmetric (top) and asymmetric (bottom) cases at $t = 130$s. The green dashed lines mark a circle of radius $r = 2$Mm. The right panels are the zoom-in views of the left ones. An animated version of this figure is available that has the same layout and runs from 0 to 400 s.

fixed at zero. The density, pressure, and B_z are fixed at their initial values. The other variables are set as outflow.

3. Simulation Results

Figure 3 shows the density distributions together with the velocity fields in the apex plane at $t = 130$s for the symmetric (top panels) and asymmetric (bottom) cases. The left column displays these quantities for a large domain while the right column zooms in on the inner portion. From Figure 3 and the associated animation, one sees that the velocity field for the symmetric case is typical of azimuthally standing kink motions. The development of vortical motions is clear at the loop boundary as a result of resonant absorption and phase mixing. For the asymmetric case, one sees the development of fan-blade-like motions propagating azimuthally. Furthermore, the velocity fields at the upper and lower loop boundaries are quite different, with small scales much easier to tell at the upper boundary.

We further demonstrate the difference of the velocity fields between the two cases by examining their radial velocities v_r. Figure 4 shows the temporal evolution of v_r along a circle of radius $r = 2$ Mm in the apex plane (the dashed lines in Figure 3). For the symmetric case (a), azimuthally
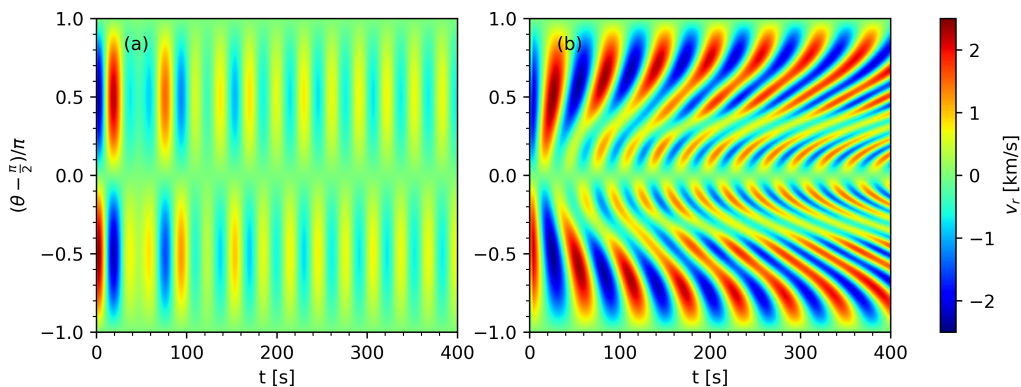
Fig. 4. Temporal evolution of the radial velocity v_r along the circle delineated in Figure 3 for (a) the symmetric and (b) asymmetric cases.
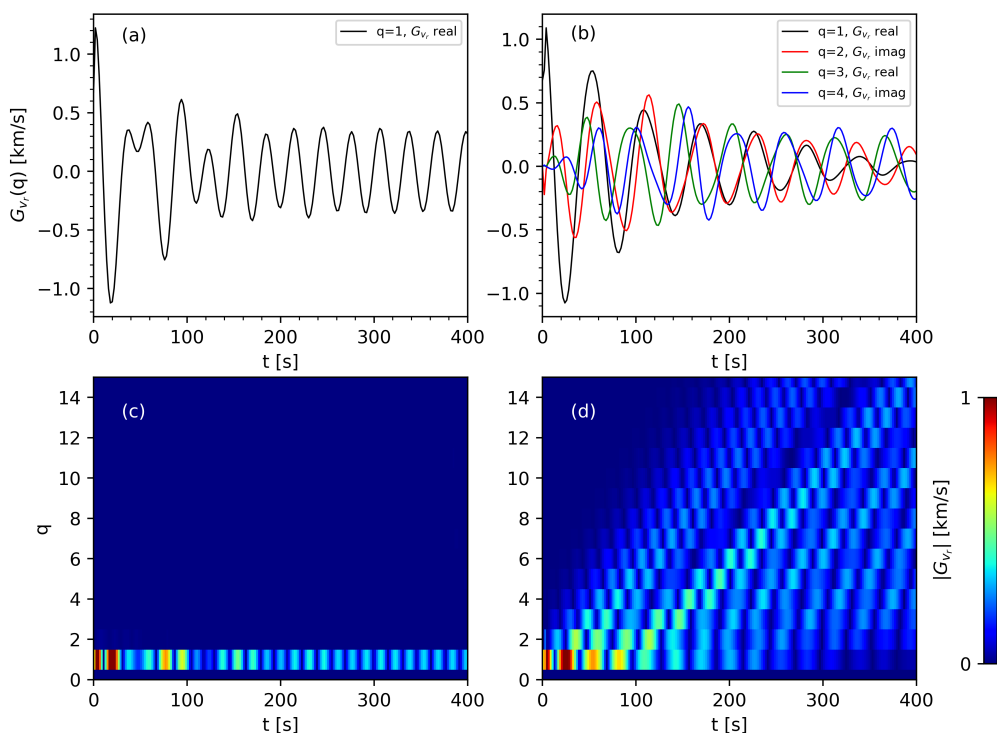

Fig. 5. Fourier coefficients G_{v_r} for the symmetric (left) and asymmetric (right) cases. Top panels show the real or imaginary part of G_{v_r} for some selected q as a function of time. Bottom panels show the modulus $|G_{v_r}|$ as a function of time and q.

standing motions are clearly shown. For the asymmetric case (b), however, v_r is seen to propagate in the azimuthal direction as the velocity stripes become increasingly inclined with time. Put another way, Fourier modes with increasingly high azimuthal wave numbers show up as time proceeds.

We then decompose the radial velocity v_r in Figure 4 into different Fourier modes. Following Terradas et al. (2018), this decomposition is performed using the discrete Fourier transform,

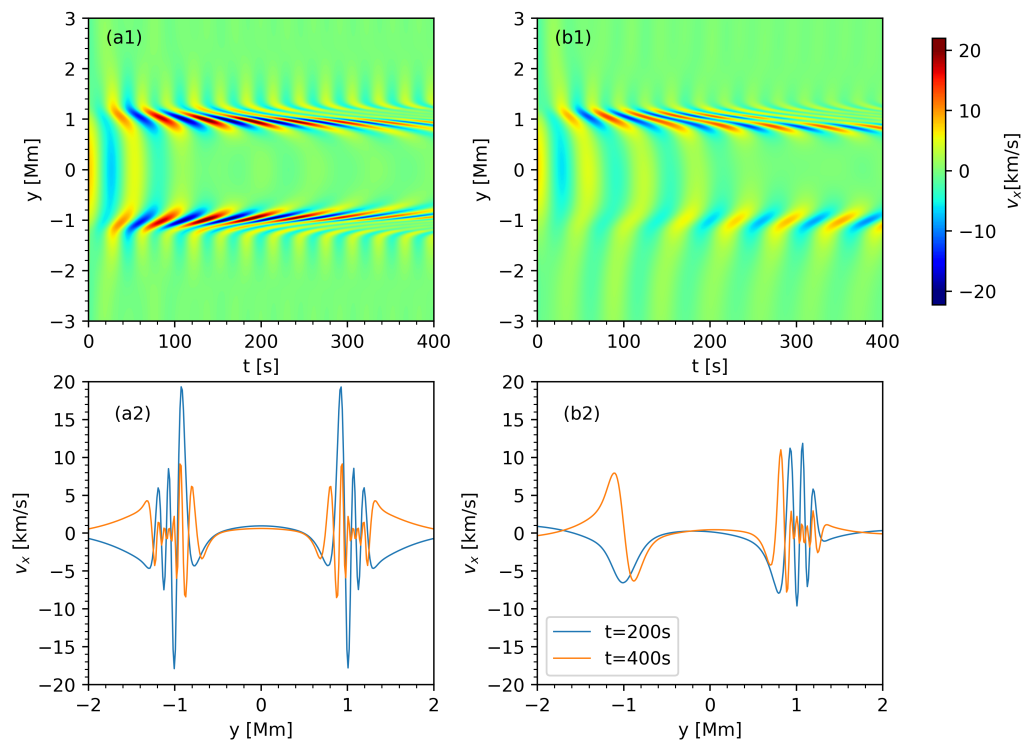$$G_{v_r}(q) = \frac{1}{N} \sum_{n=0}^{N-1} v_r(n) e^{-i \frac{2\pi n}{N} q}, \tag{4}$$

Fig. 6. Temporal evolution of $v_x(x = 0, y, z = L/2)$ for (a1) the symmetric and (b1) the asymmetric cases. The profiles of $v_x(x = 0, y, z = L/2)$ at two different times are displayed for (a2) the symmetric and (b2) asymmetric cases.

where $G_{v_r}(q)$ represents the coefficient of Fourier mode q, N is the length of the discrete v_r sequence, and $v_r(n)$ is the n-th element. Evidently, the real (imaginary) part of G_{v_r} nearly vanishes for even (odd) q given that v_r is almost symmetric about the y-axis. The Fourier coefficients as functions of q and time are displayed in Figure 5. For the symmetric case, only a single Fourier mode of $q = 1$ is recognizable, with $G_{v_r}(q = 1)$ being almost purely real (Figure 5(a)). For the asymmetric case, however, Fourier modes with higher q are excited. Figure 5(b) displays the real or imaginary parts of $G_{v_r}(q)$ for four selected Fourier modes. One finds that the Fourier coefficients of higher q modes reach their maximum at later stages, indicating the coupling among different Fourier modes. The modulus $|G_{v_r}(q)|$ as a function of q and time is displayed in the bottom panels for the (c) symmetric and (d) asymmetric cases. Similarly, one sees a single Fourier mode of $q = 1$ in the symmetric case. For the asymmetric case, multiple Fourier modes coexist and higher q modes are successively excited as time proceeds. These results demonstrate that the fan-blade-like velocity fields propagating in the azimuthal direction are attributable to the continuous excitation of higher Fourier modes and the coupling among these modes.

We have verified that wave energy is well contained in the system after a brief transient phase. Kink mode is then subject to damping due to resonant absorption and the subsequent phase mixing (Goossens et al. 2011). This process manifests itself as the vortical motions and the development of small scales at loop boundaries. The top panels of Figure 6 show the temporal evolution of v_x along the y axis in the apex plane ($z = L/2$). For the symmetric case (a1), small-scale spikes are

symmetrically developing at both sides of the loop boundary. For the asymmetric case, however, spikes develop more rapidly at the upper boundary than at the lower one. This difference is further demonstrated in the bottom panels of Figure 6, where two snapshots ($t = 200$s and 400s) of v_x are displayed. We compare our results with the theoretical prediction given by Mann et al. (1995), from which our phase mixing length L_{ph} is estimated as

$$L_{ph} = \frac{2\pi}{|\partial\omega_A/\partial y|}\frac{1}{t}, \tag{5}$$

where $\omega_A = (\pi/L)v_A(x, y)$ is the local Alfvén frequency. That small scales develop more rapidly at the upper boundary then derives from the stronger gradient in the Alfvén frequency therein. We proceed more quantitatively by evaluating the Alfvén frequencies $[\omega_{Ai}, \omega_{Ae1}, \omega_{Ae2}] \approx [0.09, 0.21, 0.11]$ rad s^{-1} with the corresponding densities. Examine the Alfvén continuum pertinent to the upper loop boundary for now. Equation (20) in Mann et al. (1995) indicates that the instantaneous phase variation across the continuum is $\Delta\varphi_1 = (\omega_{Ae1} - \omega_{Ai})t$, meaning that the number of spikes is approximately $N_{spikes,1} \approx \Delta\varphi_1/\pi$. Our setup then yields that ~ 7.6 spikes are accumulated every 200 secs, which agrees well with Figure 6b2. Likewise, one expects that ~ 1.3 extrema will be accumulated every 200 secs close to the lower loop boundary, which is also quantitatively reproduced.

The development of small scales is accompanied by the damping of coordinated kink motions. The damping envelope of kink modes has been extensively examined given their seismological potential (e.g., Ruderman & Roberts 2002; Pascoe et al. 2012; Hood et al. 2013). Here we only focus on the difference of the period and damping time for the asymmetric case from the symmetric case. Figure 7 displays the temporal evolution of v_x averaged over the region of $\rho > 0.9\rho_i$ for (a) the symmetric and (b) asymmetric cases (labeled "sym" and "asym" here). We fit the profiles using an exponentially damped sinusoid, printing the best-fit periods (P) and damping times (τ). One sees that $P_{asym} > P_{sym}$, which is unsurprising given an overall heavier ambient corona and hence a larger inertia experienced by the kink motions in the asymmetric case. That $\tau_{asym} > \tau_{sym}$ can be understood by drawing analogy with the damping of kink motions in an axisymmetric setup, for which the ideal quasi-mode theory predicts that τ/P in the thin-boundary-thin-tube (TTTB) limit decreases with the ratio of the internal density ρ_i to the ambient value ρ_{amb} (e.g., Goossens et al. 1992; Ruderman & Roberts 2002). While not straightforward to quantify, ρ_{amb} in the asymmetric case is expected to exceed ρ_{e1}, which can be unambiguously identified as ρ_{amb} in the symmetric case. That said, an exponential damping envelope does not apply to the symmetric case at large times (Figure 7a), reinforcing the notion that ideal quasi-modes offer only a partial picture for the time-dependent coordinated motions (see Soler & Terradas 2015, for details).

The profile of v_x in the symmetric case (Figure 7a) shows a beat at $t \approx 160$s. One possible cause of this beat is the interplay between kink motions and Alfvénic motions (e.g., Soler & Terradas 2015, Fig.9). It is known that the presence of similar beats may lead to an underestimation of the actual damping time (Nisticò et al. 2013). We therefore also compute the period (P_{QM}) and damping time (τ_{QM}) expected for kink quasi-modes (QMs) resonantly absorbed in the Alfvén con-
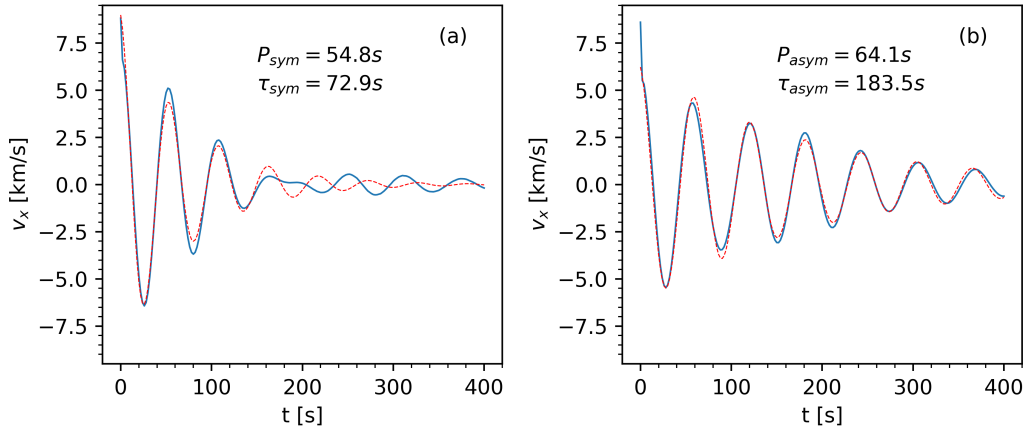
Fig. 7. Temporal profiles of v_x (averaged over the loop center with $\rho > 0.9\rho_i$) for (a) the symmetric and (b) the asymmetric cases. The red dashed lines are the best-fit exponential damped sinusoids, with the fitted period P and damping time τ displayed on each panel.
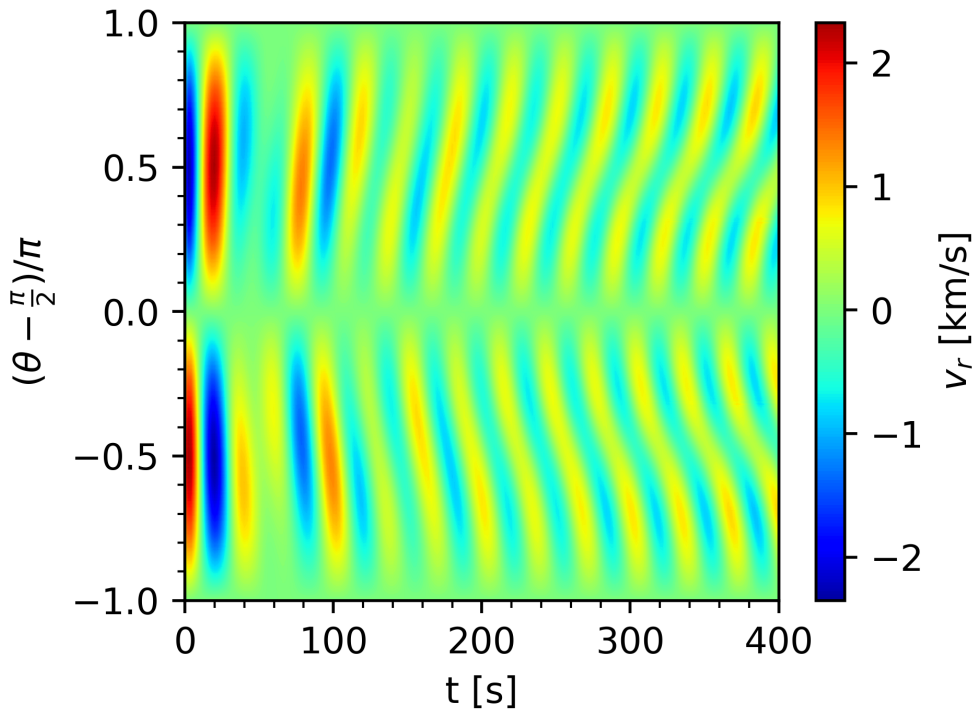

Fig. 8. Similar to Figure 4b, but for the case of $\rho_{e2} = 1.2$.

tinuum (see the review by Goossens et al. 2011, for conceptual clarifications). We specifically adapt our previous resistive eigenmode code (Chen et al. 2021) to address the present equilibrium configuration, finding that $P_{QM} \approx 51.6$ sec and $\tau_{QM} \approx 67.1$ sec. These QM values are rather close to the best-fit values in Figure 7(a)(P_{sym} and τ_{sym}), suggesting that the presence of a beat-like behavior may not significantly affect our fitting approach for evaluating the kink periods and damping times.
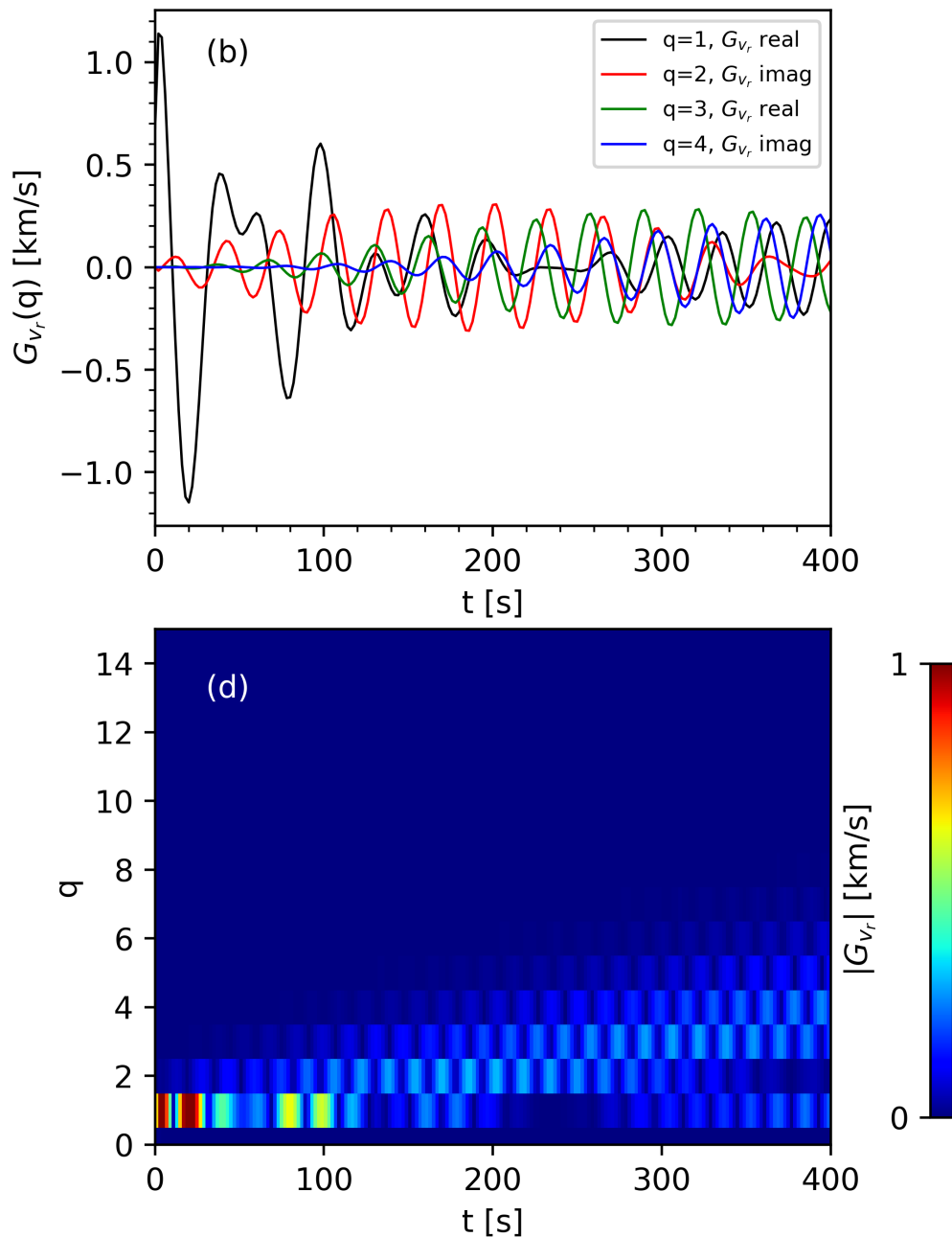
Fig. 9. Similar to the right column of Figure 5, but for the case of $\rho_{e2} = 1.2$.

In this work, we pay attention to the effect of an asymmetric loop environment on kink oscilla-tions, and thus neglect both gravity and the gravitationally stratified atmosphere in order to avoid further complexity. The density profile we adopted (Equation 2) may not quite well represent the realistic stratified density profile. In terms of modeling, however, our model makes a difference with most previous simulations where a uniform background was assumed. The results shown here are relevant for further exploring more realistic models.

It is necessary to mention that for the asymmetric case, the density variation of the environment (ρ_{e2}/ρ_{e1} = 3.5) across the loop width is more significant than the density variations over a scale height ($\Lambda \approx 50$Mm) of a 1MK corona. While we do not attempt to model a stratified density profile, we nonetheless perform an additional simulation with ρ_{e2} = 1.2. This density ratio of ρ_{e2}/ρ_{e1} = 1.2 is in line with some loops observed by TRACE or SOHO/EIT whose width w can be as large as 8Mm (e.g., Schrijver 2007), i.e., $\exp(w/\Lambda) \approx 1.2$ [1]. Similar analyses are performed, with the results being shown in Figure 8 and Figure 9. We find that the key features we previously obtained, the azimuthally propagating velocity field and the excitation of higher azimuthal Fourier modes, still exist, though not as strong as the case with ρ_{e2} = 3.5. Our model thus provides a proof-of-concept test of the effect of an asymmetric environment on kink oscillations. More realistic models taking into account both the stratified atmosphere and the gravity effect are called for.

4. Summary

We studied kink modes supported by a straight coronal loop in an asymmetric environment using 3D MHD simulations. The new features compared with the case of symmetric ambients are summarized as follows:

1) The velocity fields in the exterior shows the development of fan-blade features that propagate azimuthally. This is attributed to the successive excitation of higher azimuthal Fourier modes.
2) Resonant absorption and phase mixing can still occur in the asymmetric case. Velocity spikes are generated nonsymmetrically, with small scales developing more rapidly at the upper boundary than at the lower.

This work provides a simplified model studying horizontally polarized kink modes supported by coronal loops in an asymmetric ambient corona. These findings enrich our understanding of kink modes in more realistic configurations and are helpful for future high-resolution observations.

References

Allcock, M. & Erdélyi, R. 2017, Sol. Phys., 292, 35

Anfinogentov, S. A., Nakariakov, V. M., & Nisticò, G. 2015, A&A, 583, A136

Antolin, P., Okamoto, T. J., De Pontieu, B., et al. 2015, ApJ, 809, 72

Arregui, I., Andries, J., Van Doorsselaere, T., Goossens, M., & Poedts, S. 2007, A&A, 463, 333

Aschwanden, M. J., Fletcher, L., Schrijver, C. J., & Alexander, D. 1999, ApJ, 520, 880

Banerjee, D., Krishna Prasad, S., Pant, V., et al. 2021, Space Sci. Rev., 217, 76

Chen, S.-X., Li, B., Guo, M., Shi, M., & Yu, H. 2022, ApJ, 940, 157

Chen, S.-X., Li, B., Van Doorsselaere, T., et al. 2021, ApJ, 908, 230

---

[1] Note that a nominal loop radius R = 1 Mm serves essentially as a normalizing constant in our gravity-free modeling. The key dynamics here results primarily from the deviation of the dimensionless ρ_{e2}/ρ_{e1} from unity. As such, the ensuing results are equally applicable upon proper scaling (see Sect.4.1.2 in Goedbloed et al. 2019, for more on this aspect).

De Moortel, I. & Howson, T. A. 2022, ApJ, 941, 85

Edwin, P. M. & Roberts, B. 1983, Sol. Phys., 88, 179

Goddard, C. R. & Nisticò, G. 2020, A&A, 638, A89

Goddard, C. R., Nisticò, G., Nakariakov, V. M., & Zimovets, I. V. 2016, A&A, 585, A137

Goedbloed, H., Keppens, R., & Poedts, S. 2019, Magnetohydrodynamics of Laboratory and Astrophysical Plasmas (Cambridge University Press)

Goossens, M., Erdélyi, R., & Ruderman, M. S. 2011, Space Sci. Rev., 158, 289

Goossens, M., Hollweg, J. V., & Sakurai, T. 1992, Sol. Phys., 138, 233

Guo, M., Li, B., & Van Doorsselaere, T. 2020, ApJ, 904, 116

Guo, M., Van Doorsselaere, T., Karampelas, K., et al. 2019, ApJ, 870, 55

Hood, A. W., Ruderman, M., Pascoe, D. J., et al. 2013, A&A, 551, A39

Karampelas, K., Van Doorsselaere, T., & Antolin, P. 2017, A&A, 604, A130

Li, B., Antolin, P., Guo, M. Z., et al. 2020, Space Sci. Rev., 216, 136

Magyar, N. & Van Doorsselaere, T. 2016, A&A, 595, A81

Mann, I. R., Wright, A. N., & Cally, P. S. 1995, J. Geophys. Res., 100, 19441

Mignone, A., Bodo, G., Massaglia, S., et al. 2007, ApJS, 170, 228

Miyoshi, T. & Kusano, K. 2005, Journal of Computational Physics, 208, 315

Nakariakov, V. M., Anfinogentov, S. A., Antolin, P., et al. 2021, Space Sci. Rev., 217, 73

Nakariakov, V. M. & Ofman, L. 2001, A&A, 372, L53

Nakariakov, V. M., Ofman, L., Deluca, E. E., Roberts, B., & Davila, J. M. 1999, Science, 285, 862

Nisticò, G., Nakariakov, V. M., & Verwichte, E. 2013, A&A, 552, A57

Pascoe, D. J., Hood, A. W., de Moortel, I., & Wright, A. N. 2012, A&A, 539, A37

Ruderman, M. S. & Roberts, B. 2002, ApJ, 577, 475

Schrijver, C. J. 2007, ApJ, 662, L119

Shi, M., Van Doorsselaere, T., Antolin, P., & Li, B. 2021a, ApJ, 922, 60

Shi, M., Van Doorsselaere, T., Guo, M., et al. 2021b, ApJ, 908, 233

Soler, R. & Terradas, J. 2015, ApJ, 803, 43

Terradas, J., Magyar, N., & Van Doorsselaere, T. 2018, ApJ, 853, 35

Tian, H., McIntosh, S. W., Wang, T., et al. 2012, ApJ, 759, 144

Tomczyk, S., McIntosh, S. W., Keil, S. L., et al. 2007, Science, 317, 1192

Van Doorsselaere, T., Nakariakov, V. M., & Verwichte, E. 2008, ApJ, 676, L73

Van Doorsselaere, T., Srivastava, A. K., Antolin, P., et al. 2020, Space Sci. Rev., 216, 140

Wang, T., Ofman, L., Davila, J. M., & Su, Y. 2012, ApJ, 751, L27

Wang, T., Ofman, L., Yuan, D., et al. 2021, Space Sci. Rev., 217, 34

Wang, T. J., Solanki, S. K., & Selwa, M. 2008, A&A, 489, 1307

Yang, Z., Bethge, C., Tian, H., et al. 2020, Science, 369, 694

Zimovets, I. V. & Nakariakov, V. M. 2015, A&A, 577, A4

Zsámberger, N. K., Allcock, M., & Erdélyi, R. 2018, ApJ, 853, 136